Showcasing research from Professor Yang's laboratory, Hunan Key Laboratory of Mineral Materials and Application, School of Minerals Processing and Bioengineering, Central South University, Changsha, China

A nanoclay-based 3D aerogel framework for flexible flame retardants

A ternary interpenetrating flexible flame retardant aerogel assembled by nanoclay-based nanosheets was synthesized. Its horizontal 3D structure and radial wave-shape layer ensure its outstanding compression resilience, bendability, and foldability. Nanoclay-based nanosheets as thermal and qualitative insulator could significantly improve flame retardancy.
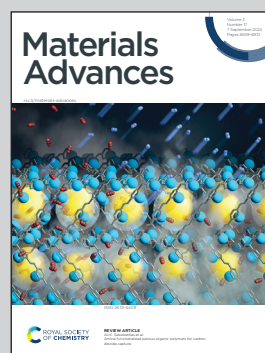
ROYAL SOCIETY OF CHEMISTRY

rsc.li/materials-advances

PAPER

Check for updates

A nanoclay-based 3D aerogel framework for flexible flame retardants†

Weimin Xie,[a] Jie Wang,[a] Kaixuan Shang,[a] Hongyun Chen,[a] Aidong Tang,[b] Mingjie Wu,[c] Xun Cui [ID][def] and Huaming Yang [ID] *[adef]

The rational design and facile synthesis of flame-retardant aerogels featuring superior compressibility and favorable flexibility are crucial for green advanced buildings and soft decoration but remain challenging due to the general inaccessibility of both high flame retardancy and good flexibility. Herein, we report a facile route to crafting an emerging ternary crosslinked composite aerogel with an interpenetrating three-dimensional (3D) network structure *via* employing cellulose-dispersed nanoclay (*i.e.*, rectorite) (CR) as both a 3D skeleton and a flame-retardant component and organic polyaniline (PA) and polyvinyl alcohol (PVA) as a flexibilizer and a crosslinker, respectively. Specifically, a stable rectorite suspension is first prepared by introducing cellulose nanocrystals to alleviate the agglomeration of rectorite nanosheets. Subsequently, the *in situ* polymerization of PA on the surface of the obtained CR nanosheets and the addition of PVA lead to the formation of a ternary network aerogel (denoted as CR/PA/PVA). Impressively, the horizontal 3D structures and radial wave-shape layers of CR/PA/PVA ensure outstanding compression resilience, bendability, and foldability. Remarkably, CR nanosheets as a thermal and qualitative insulator significantly improve the peak heat release rate (as low as 8.3 kJ m^{-2}) of CR/PA/PVA, outperforming most state-of-the-art flame-retardant products. As such, the rationally designed interpenetrating 3D network structured CR/PA/PVA offers a unique platform for developing high-performance flexible flame retardants.

Introduction

With the increasing awareness of public safety, people put forward higher requirements for the flame retardant materials which are commonly used in daily life. In particular, the mechanical resilience and flexibility of these materials are highly desirable for practical applications.[1–4] As a kind of typical compressible and flexible materials, polymeric aerogels have attracted considerable attention due to their unique properties, including good flexibility, high porosity, large specific surface area, and low density.[5–7] However, despite these encouraging features, most of these materials are easy to be ignited, and the flame could rapidly spread in the absence of a fire barrier. Recent advances have demonstrated that the flame-retardant properties of organic/inorganic composite aerogels can be significantly improved by incorporating uniformly distributed inorganic fillers (*e.g.*, silica, clay, graphene, carbon nanotubes, metal oxides, and hydroxides) to delay the transfer of heat.[8–10] Nonetheless, the incorporation of these inorganic fillers to organic materials generally results in more brittle hybrids, significantly limiting their scope of applications.[11,12] Furthermore, the poor compatibility between inorganic fillers and polymer matrices often leads to catastrophic disintegration during the combustion process and fails to prevent the heat-induced collapse of the building.[13,14] Moreover, the commonly employed preparation approaches for these composite aerogels such as hydrothermal and solvent exchange are usually uncontrollable to some extent. In this context, developing novel strategies to controllably synthesize such composite aerogels with both excellent flame retardancy and mechanical properties represents an important endeavour toward high-efficiency flexible flame retardants.

Tetrahedral silicon oxide and octahedral Al, Fe or Mg oxides, which constitute natural layer-structured clay minerals, are the

a Hunan Key Laboratory of Mineral Materials and Application, School of Minerals Processing and Bioengineering, Central South University, Changsha 410083, China

b College of Chemistry and Chemical Engineering, Central South University, Changsha 410083, China

c Electrochemistry/Corrosion Laboratory, Department of Chemical Engineering, McGill University, Montréal, Québec H3A 0C5, Canada

d Engineering Research Center of Nano-Geomaterials of Ministry of Education, China University of Geosciences, Wuhan 430074, China.
E-mail: hm.yang@cug.edu.cn, hmyang@csu.edu.cn

e Faculty of Materials Science and Chemistry, China University of Geosciences, Wuhan 430074, China

f Key Laboratory of Functional Geomaterials in China Nonmetallic Minerals Industry, China University of Geosciences, Wuhan 430074, China

† Electronic supplementary information (ESI) available. See DOI: https://doi.org/10.1039/d2ma00556e

main components of the commonly used flame retardants.[15,16] Accordingly, these clay minerals are impermeable to heat and gas molecules, thereby extending the heat propagation path.[17,18] Furthermore, the low cost, easy processing, environmental friendliness and excellent biocompatibility of these materials have attracted much attention in the context of flame retardants.[19,20] Particularly, rectorite nanoclay which composed of dioctahedral mica layers and dioctahedral montmorillonite layers stacked in a ratio of 1:1 has demonstrated excellent thermal stability and extremely high fire-resistance temperature (*i.e.*, melting point; up to 1660 °C) due to its certain aspect ratio and unique structure that the mica layer is included between the interlayers.[21] As a result, rectorite can serve as the thermal and qualitative insulator and show relatively higher flame retardancy than other clay minerals.[22,23] Nonetheless, due to the poor dispersion of rectorite, the rectorite interlayer may be severely aggregated in polymer matrices, thereby deteriorating the performance of aerogels.[24,25] Very recently, cellulose nanocrystals with good water dispersibility have been proposed to be capable of adequately dispersing rectorite and preventing rectorite from excessively restacking in aqueous solution.[2] It is notable that the well dispersed nanorectorite could simultaneously act as supporters to improve the mechanical strength of aerogels. Besides, organic flexible polyaniline (PA) which composed of alternative amine and imine groups in its backbone has been demonstrated to act as a coupling agent to form covalent bonds between PA and polyvinyl alcohol (PVA), resulting in significantly improved interfacial interactions and increased dispersion of nanoparticles in the polymer matrix.[26,27] Also, PA itself is reported to be a good flame retardant.[28] Furthermore, the addition of a certain amount of PVA as an adhesive could undoubtedly improve the stability and adjustability of the aerogel *via* solidifying the junctions between the components through their abundance of inherent hydroxyl groups.[29] Note that the incorporation of PA and PVA could further enhance the flame retardance of polymer composites due to their carbon-forming ability.[30] Clearly, the capability of creating rectorite/PA/PVA ternary crosslinked composite aerogels may enable the construction of efficient flame retardants with enhanced compressibility and flexibility.

Herein, we demonstrate a facile one-pot *in situ* polymerization strategy to crafting an emerging ternary crosslinked composite aerogel with an interpenetrating 3D network structure *via* employing cellulose-dispersed rectorite (CR) as both the 3D skeleton and the flame-retardant component and organic PA and PVA as the flexibilizer and crosslinker, respectively. Specifically, a stable rectorite suspension is first prepared by introducing cellulose nanocrystals to weaken the agglomeration of rectorite nanosheets. The following *in situ* polymerization of PA on the surface of the obtained CR nanosheets and the addition of PVA lead to the formation of a ternary network aerogel (denoted as CR/PA/PVA). To study the effect of the surface groups of rectorite nanosheets on the morphology and structure of the aerogel, the rectorite was calcined to determine the role of the hydroxyl groups on the surface of the rectorite. Benefiting from the horizontal 3D network structures and radial wave-shape layers, the as-prepared CR/PA/PVA

aerogel exhibits not only outstanding flame-retardant properties but also excellent flexibility in both compression and bending, with compressibility over 80% strain and bending without fractures. This work is expected to expand the practical applications of rectorite-based aerogels in green advanced buildings and soft decoration fields.

Experimental

Materials

The pristine rectorite nanoclay used in this study was provided by Hubei Zhongxiang Mingliu Rectorite Development Co., Ltd, (Hubei Province, China). An aqueous suspension of cellulose nanocrystals (8.0 wt%) was supplied by Guilin Qihong Technology Co., Ltd (China), which was hydrolyzed from metasequoia pulp by hydrochloric acid, catalyzed by sodium hydroxide, and then obtained by the carboxymethylation reaction with chloroacetic acid. Finally, the cellulose nanocrystals have a length of 0.1–0.5 μm and a diameter of 3–10 nm. Ammonium persulfate (98% purity, M_w = 228.20 g mol^{-1}), aniline (pure, d = 1.022 g mL^{-1}, M_w = 93.13 g mol^{-1}), phosphoric acid (H_3PO_4, 85 wt%), and PVA (M_w = 145 000) were purchased from Shanghai Sinopharm Chemical Reagent Co. (China). All reagents were used without further purification. The PVA solution was prepared by dissolving PVA particles in deionized water at 90 °C by stirring for 4 h. The concentration of the PVA solution prepared experimentally was 10%.

Thermal treatment of rectorite

To study the effect of the surface groups of rectorite on the properties of the resultant aerogels, the pristine rectorite was treated in a muffle furnace from room temperature (RT) to the design temperatures (300 °C, 450 °C, and 900 °C) at a heating rate of 10 °C min^{-1} and kept for 2 h. Scanning electron microscope (Fig. S1, ESI†), images revealed that most of the rectorite presented an obvious two-dimensional layered structure. As the calcination temperature increases, the layer structure still maintained even at 900 °C.

The preparation of CR/PA/PVA-x composite aerogels

CR/PA/PVA-x aerogels were synthesized from rectorite nanoclay, aniline, and PVA *via* an *in situ* polymerization and a following freeze-drying process. To study the effect of the surface groups of rectorite nanosheets on the properties of the resultant aerogels, CR/PA/PVA-x (x = RT, 300, 450, and 900) aerogels were also synthesized by adjusting the calcination temperatures (300 °C, 450 °C, and 900 °C, respectively) of rectorite, and the RT refers to room temperature rectorite. In a typical synthesis procedure of CR/PA/PVA-RT, 12.5 g of 8 wt% cellulose nanocrystals and 8 g of rectorite were first mixed in 287.5 g of deionized water; after overnight mechanical stirring and ultrasonic treatment for 0.5 h, a uniformly dispersed rectorite suspension (*i.e.*, CR) can be obtained. Next, a specific amount of H_3PO_4 was added to the above mixture so that the molar concentration was 1 M, followed by adding 0.2 g of the aniline

monomer and stirred for 1 h in an ice bath. After this, an ammonium persulfate aqueous solution (a mass ratio of aniline monomer to ammonium persulfate is 4 : 3) was added dropwise to initiate the *in situ* polymerization. The entire polymerization process was conducted in an ice bath below 5 °C by continuous mechanical stirring and sonication until the colour of the solution was no longer changed (dark green). Subsequently, 80 g of 10% PVA solution was added, and the entire mass of the final solution was 400 g. Finally, the resulting mixed solution was freezed at −55 °C and dried under vacuum conditions (1 Pa) for 72 h to obtain the CR/PA/PVA-RT aerogel. CR/PA/PVA-300, CR/PA/PVA-450, and CR/PA/PVA-900 were also synthesized using similar procedures. As a control, the same procedure was used to synthesize the C/PA/PVA aerogel without rectorite. In addition, we have synthesized the sample without PA and without the *in situ* synthesis of PA as the reference (Fig. S2, ESI†). The prepared aerogel has poor mechanical properties, lacks flexibility and elasticity, and has obvious cracks on the surface of the material, which is easy to break, so its flame retardant properties and mechanical properties are not further tested.

Characterization

The morphology of the composite aerogels was observed by field-emission SEM (Mira3 LMU) equipped with energy-dispersive spectrometry (EDS) at an accelerating voltage of 8 kV. Transmission electron microscopy images were obtained using a JEOL JEM-2100F microscope operating at 200 kV. The aerogels with a size of $10 \times 10 \times 15$ mm^3 were prepared for compression testing, which was conducted using a CMT 6103 testing machine at a speed of 10.0 mm min^{-1} with a 1000 N load cell. All thermal images were taken using an infrared camera (Fluke, Ti55) at ambient temperature (approximately 25 °C); the temperature variation was recorded in real-time. The combustion behaviors of the CR/PA/PVA aerogels and the C/PA/PVA aerogel were measured using an FTT0007 cone calorimeter. Samples with sizes of 100 mm × 100 mm × 15 mm were tested at a heat flux of 50 kW m^{-2}. The thermal conductivity of the aerogels was measured by the steady-state hot-wire method using a XIA-TECH thermal conductivity meter. The thermogravimetric and differential scanning calorimetry analyses (TG/DSC) of the aerogels were carried out using a Mettler-Toledo TG DSC3+ 1600LF thermal analyzer (Zurich, Switzerland) under an air atmosphere at a heating of 10 °C min^{-1}. Wide-angle X-ray diffraction patterns were obtained using a Rigaku ultimate IV diffractometer at a scanning rate of 2° min^{-1} and a 2θ range of 2–80°. Fourier transform infrared spectroscopy (FTIR) measurements were taken using a Nicolet Nexus 670 FTIR spectrophotometer from 4000 to 400 cm^{-1} at a resolution of 4 cm^{-1}.

Results and discussion

Preparation of CR/PA/PVA composite aerogels

As schematically illustrated in Fig. 1, the general synthetic route to the ternary CR/PA/PVA aerogels involves the cellulose nanocrystal-assisted dispersion of rectorite nanosheets (*i.e.*, CR)

followed by the *in situ* polymerization of PA on the surface of the obtained CR and the addition of PVA to obtain the target CR/PA/PVA aerogel with an interpenetrating 3D network architecture. Specifically, the CR nanosheets were used as the major building blocks to provide polymers with crosslinking sites and to block heat transfer. Generally, the rectorite nanosheets tend to aggregate easily and thus exhibit poor dispersion in the matrix due to the strong interaction between the interlayers of rectorite (Fig. 1(A)–(C)). In sharp contrast, when rectorite was added to the cellulose nanocrystal (Fig. 1(I) and (J)) hydrogel, the dispersion of rectorite can be markedly improved (Fig. 1(K)). Compared with the pristine rectorite, the crystalline structure of the cellulose-dispersed rectorite (*i.e.*, CR) remained essentially unchanged (ESI,† Fig. S3).[18] Subsequently, aniline and ammonium persulfate were used as the monomer and initiator, respectively, to *in situ* synthesize PA on the surface of the obtained CR nanosheets. The following successive addition and mixture of PVA as well as freeze-drying treatment obtained the flame-retardant ternary CR/PA/PVA network aerogel with high flexibility (Fig. 1(D)–(H)). Note that the increased number of crosslinking sites by the incorporation of cellulose nanocrystals could enhance the interfacial interactions between the rectorite nanosheet and the polymer matrix during mechanical stirring, thus improving the strength of the final aerogel. Significantly, benefiting from the abundance of surface hydroxyl groups and the simplicity of the one-pot synthesis route, the target CR/PA/PVA aerogel can be easily produced in large quantities (Fig. S4, ESI†).

Mechanical properties and morphology characterization

The as-prepared CR/PA/PVA-RT bulk aerogels are shown in Fig. 2(A). The densities of the CR/PA/PVA-RT, CR/PA/PVA-300, and CR/PA/PVA-450 aerogels were found to be 0.105, 0.1074 and 0.1193 g cm^{-3}, respectively. Since the surface groups of rectorite are less destroyed during calcination at low temperatures (<500 °C) (Fig. S5, ESI†), the CR/PA/PVA-RT, CR/PA/PVA-300, and CR/PA/PVA-450 aerogels show similar mechanical properties. Therefore, the CR/PA/PVA-RT composite aerogel is selected for the mechanical performance test considering energy conservation. As displayed in Fig. 2(B), the CR/PA/PVA-RT composite aerogel (10 mm × 10 mm × 20 mm) can be reversibly compressed and released, manifesting attractive compressibility. In addition to high compressibility, the CR/PA/PVA-RT composite aerogel also exhibits extremely high flexibility and can withstand a large curling deformation without any cracking (Fig. 2(C)–(G)). Even when the CR/PA/PVA-RT composite aerogel is tailored into strips, the aerogel can be knotted into any shape and coiled around a rod ($\varphi = 5$ mm). Owing to the above-mentioned excellent flexibility, the CR/PA/PVA-RT composite aerogel can also be folded arbitrarily at least twice without rupture at a curvature radius of ≈ 1 mm.

The mechanical behaviours of these aerogels are essential properties for almost all applications. Therefore, typical compressive stress–strain (σ–ε) measurements were carried out to quantitatively evaluate the mechanical properties of CR/PA/PVA-x composite aerogels as shown in Fig. 2(H)–(J). Since the
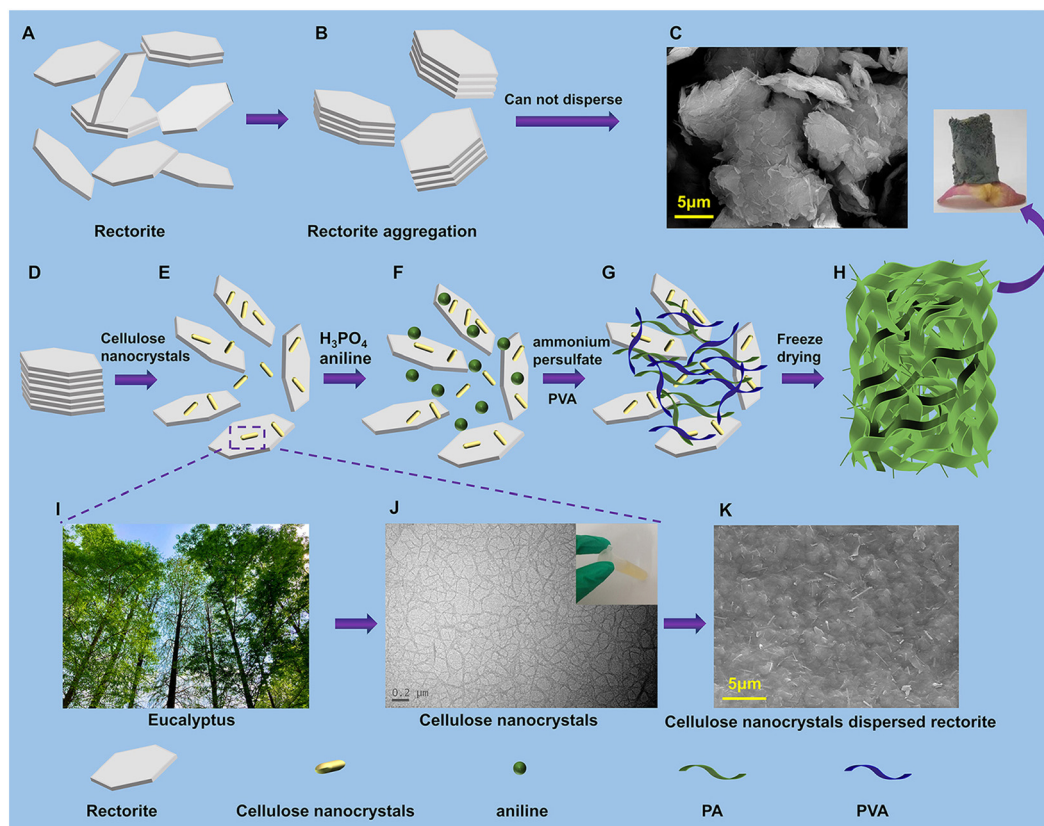
Fig. 1 (A) and (B) Schematic of the agglomeration of the pristine rectorite. (C) SEM image of the pristine rectorite. (D)–(H) Schematic diagram of the preparation process of the CR/PA/PVA aerogel. (I) Photograph of metasequoia. (J) TEM image of cellulose nanocrystals. (K) SEM image of rectorite dispersed by cellulose nanocrystals.

C/PA/PVA (control sample) aerogel without rectorite exhibits a film-like structure rather than a 3D network structure, the stress–strain was not investigated. It is evident that the CR/PA/PVA-RT and CR/PA/PVA-900 aerogels exhibit excellent compression behaviours at an 80% strain (Fig. S6, ESI†). For the CR/PA/PVA-RT aerogel, rectorite has the most abundant surface groups, so it is more firmly bound to the PA and PVA molecular chains, and forms a 3D network structure through cross-linking, thus the compressive stress is greater. Besides, the compressive strength of the CR/PA/PVA-900 aerogel can reach up to 440 kPa, which is attributed to their lack of three-dimensional porous structure and high density. Fig. 2(I) shows the compressive stress–strain curves of CR/PA/PVA aerogels at a strain of 50%. Similarly, the CR/PA/PVA-RT and CR/PA/PVA-900 aerogels also exhibit greater stress. However, the compression–decompression test curves at a 50% strain of CR/PA/PVA-900 is not closed, indicating that its elasticity is poor. Furthermore, the cyclic compression test was performed (Fig. 2(J) and Movie S1, ESI†), which displays compressive stress *versus* strain curves obtained from the compression and decompression tests of the CR/PA/PVA-RT aerogel with the strain ranging from 20% to 80%. The compressive stress–strain curves can be divided into three characteristic deformation regions: a plateau region ($\varepsilon < 20\%$), a linear elastic region ($20\% < \varepsilon < 60\%$), and a steep slope region ($\varepsilon > 60\%$). Interestingly, the CR/PA/PVA-RT

aerogel could perfectly recover its original heights after removing the force. The key factor in the flexibility of CR/PA/PVA-RT composite aerogels can be ascribed to the 3D spatial structure connected among PA, PVA, and CR, which act as "buffer regions" to dissipate external stress and generate large deformations. The superior mechanical flexibility of the composite aerogel allows mechanical compliance with the surfaces of the arbitrary substrate undergoing compressing, bending, and even folding in practical use.

This microscopic structure of the aerogel samples was characterized by the scanning electron microscopy (SEM) observation. A 3D network structure was observed in the horizontal direction in CR/PA/PVA-RT (Fig. 3(A)), CR/PA/PVA-300 (Fig. 3(B)), and CR/PA/PVA-900 (Fig. 3(C)). Highly tightly packed pore microstructures with a size range of 50–100 μm are noted for CR/PA/PVA-RT and CR/PA/PVA-300. However, CR/PA/PVA-900 displays a collapsed 3D structure and fewer pore structures can be observed, so its density is higher, of 0.3255 g cm^{-3}. This may be due to a certain aggregation of the composites caused by the destruction of the surface groups of rectorite after being calcined at 900 °C (Fig. S5, ESI†), which can be verified by the FTIR spectra of CR/PA/PVA aerogels (Fig. S7, ESI†). With the increase of the calcination temperature of the rectorite, the peak intensity corresponding to the surface groups decreases, and the crosslinking effect weakens. Note that the C/PA/PVA aerogel without rectorite
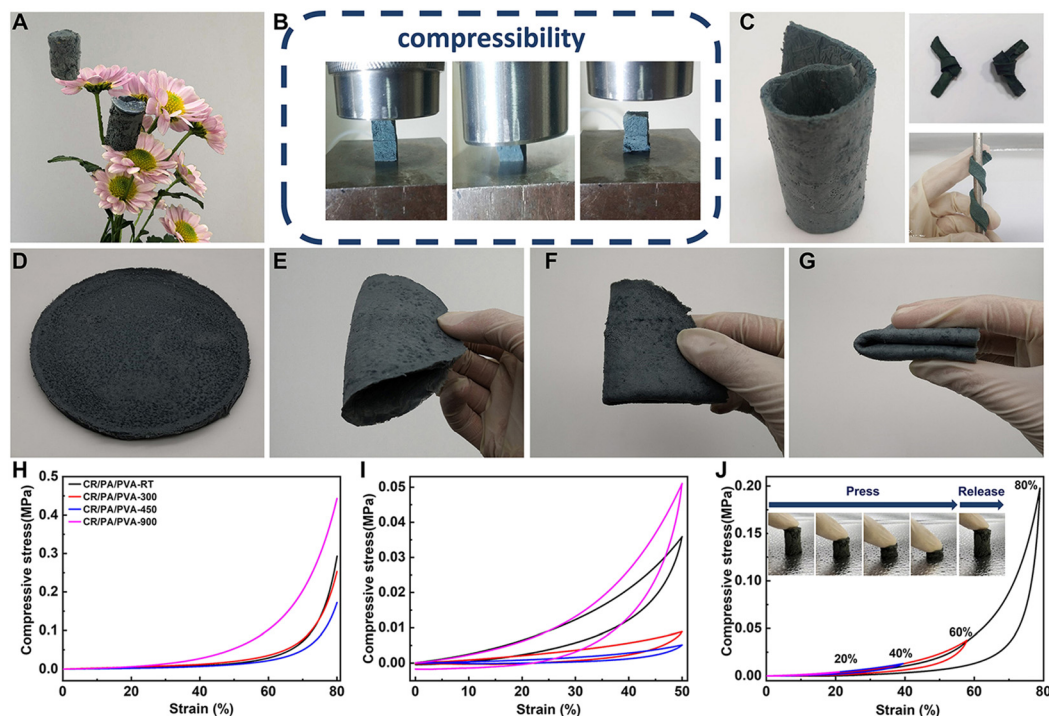
Fig. 2 Mechanical properties of resultant aerogels. (A) Piece of the CR/PA/PVA-RT aerogel standing on petals. (B) Compressibility. (C) Flexibility. (D)–(G) Foldability of the CR/PA/PVA aerogel. Mechanical properties of the CR/PA/PVA aerogel. (H) Compressive stress−strain curves with compressive behaviour at 80% strain. (I) Compressive stress−strain curves of compression−decompression tests at 50% strain. (J) Compressive stress−strain curves of the CR/PA/PVA-RT aerogel at 20%, 40%, 60%, and 80% strain. The inset shows the photographs of the compression−decompression test of CR/PA/PVA-RT.
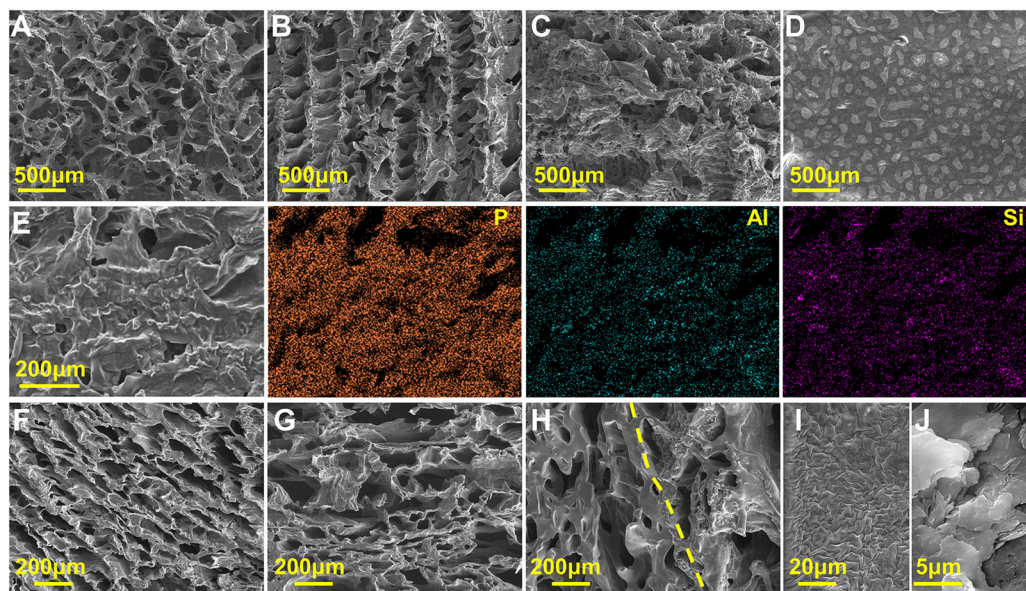
Fig. 3 Scanning electron microscopy (SEM) images of the aerogels. Horizontal images of (A) CR/PA/PVA-RT, (B) CR/PA/PVA-300, (C) CR/PA/PVA-900 and (D) C/PA/PVA aerogels. (E) SEM image and corresponding EDX elemental mappings (P, Al, and Si) of the CR/PA/PVA-RT aerogel. Cross-section SEM images of (F) CR/PA/PVA-RT, (G) CR/PA/PVA-300 and (H)−(J) CR/PA/PVA-900 aerogels.

exhibits a film-like structure rather than a 3D structure (Fig. 3(D)). Furthermore, the energy dispersive X-ray (EDX) elemental mapping analysis on CR/PA/PVA-RT (Fig. 3(E)) confirms a uniform distribution of P, Si, and Al elements. Notably, phosphoric acid is used as a dopant for PA to introduce phosphate groups into the composite, imparting more excellent flame retardancy to the
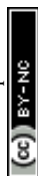
resulting composite aerogels.[31,32] Besides, the continuous wave-shape layers can be observed from the cross-sections of CR/PA/PVA-RT and CR/PA/PVA-300 (Fig. 3(F) and (G)). This may be because:[2] upon ice formation and directional growth during freezing, the rectorite nanosheets and CNCs are rejected by the ice crystals to form a lamellar structure. Meanwhile, the thin lamellas are crumpled into wave-shape layers by ice crystals. Based on the above results, it is suggested that the 3D network structure contributes to the mechanical properties of the final composite aerogels.

However, the CR/PA/PVA-900 aerogel undergoes an irreversible deformation. The cross-section of CR/PA/PVA-900 shows obvious delamination (Fig. 3(H)–(J)). The upper layer is an organic layer and the lower layer is a clay layer, which explains why CR/PA/PVA-900 has high compressive strength and poor elasticity. In fact, the hydroxyl group of rectorite are removed at 900 °C, so that it cannot be tightly crosslinked with PA and PVA by chemical bonds. In addition, the as-prepared CR/PA/PVA-RT aerogel can support 10 kN pressure at approximately 80% compressive strain, and exhibits good recovery (Fig. S4A–D and Movie S2, ESI†). From the perspective of mechanics, the wave-shape structure can maintain a large out-of-plane deformation and a small in-plane strain.[33] Therefore, the architecture can undergo the large deformation and restore its original

shape even at high strain without destroying the structure. Combined with the above discussions, the compression and elasticity mechanisms of the CR/PA/PVA composite aerogels are proposed (Fig. S4E–H, ESI†). The wave-shape architecture and large space among these wave layers guarantee high compressibility, and the 3D network of PA and PVA creates strong interactions among rectorite nanosheets, thus forming a flexible layer with reversible motion and resulting in superior stability and elasticity.

Fire resistance and heat insulating test

The combustion behaviours of the CR/PA/PVA composite aerogel and the control sample (*i.e.*, C/PA/PVA) were investigated by cone calorimetry, as their flammability could be better evaluated from a thermodynamic perspective. The results include ignition time, heat-release rate, peak heat-release rate, total heat release, and total smoke release (Fig. 4(A)–(C), Table S1, and Movies S3, S4, ESI†). It is worth noting that the ignition time refers to the time required for the sample to ignite at the required heat flux of the cone calorimeter. The ignition time of the CR/PA/PVA composite aerogel is significantly increased compared with that of C/PA/PVA, which is probably due to the rectorite itself being non-combustible and having a certain aspect ratio. Simultaneously, the heat-release rate, total heat
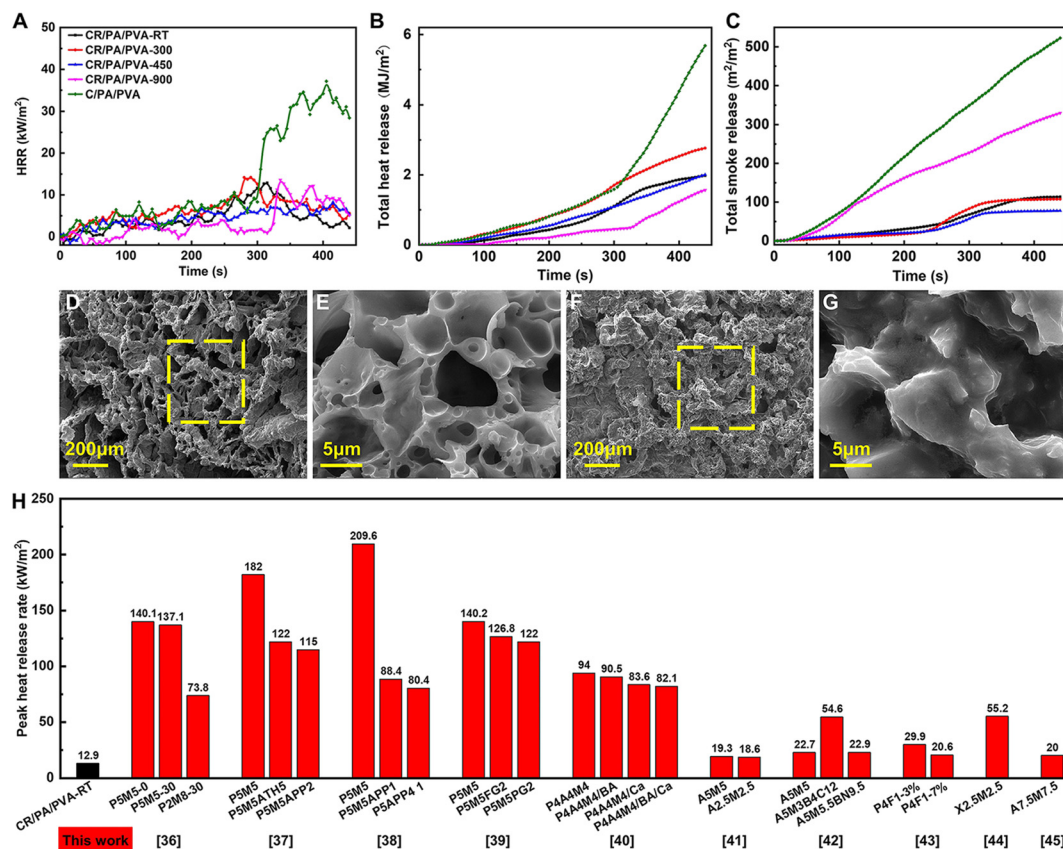

Fig. 4 Combustion behaviours of the obtained aerogels as a function of burning time. (A) Heat-release rate, (B) total heat release, and (C) total smoke release. SEM images after burning with a cone calorimeter: (D) and (E) CR/PA/PVA-RT and (F) and (G) CR/PA/PVA-900. (H) Comparison of the flame-retardant properties of the CR/PA/PVA-RT aerogel with other clay-based (mainly montmorillonite) composite aerogels.

release, and total smoke release are all reduced with the incorporation of rectorite in the C/PA/PVA composite aerogel. Notably, the total smoke release of CR/PA/PVA-RT is reduced from 522.7 $m^2 m^{-2}$ of C/PA/PVA without rectorite to 70 $m^2 m^{-2}$, a significant decrease of approximately 8 times. The introduction of rectorite could improve the thermal stability of aerogels, resulting in a less release of smoke precursors. In addition, the rectorite can promote the formation of a compact carbon layer to prevent combustible gases from diffusing into air and increase the residual weight of aerogels. Thus, the flame-retardant effect of the CR/PA/PVA aerogel is improved, especially in reducing the negative impact of organic matter decomposition, which can sharply mitigate the amount of smoke generated and reduce the heat-release-rate value of the composite aerogels. For the CR/PA/PVA-900 aerogel, due to the destruction of the surface groups of the rectorite, the cross-linking effect is weak and an obvious delamination structure is formed (Fig. 3(H)–(J)), and a dense carbon protective layer cannot be formed during the combustion process; so a lot of heat and smoke are released by the polymer molecules release during combustion.

The thermogravimetric and differential scanning calorimetry analyses (TG/DSC) indicate that the CR/PA/PVA-RT, CR/PA/PVA-300 and CR/PA/PVA-450 aerogels exhibit better thermal stability, with about 40% weight loss at 800 °C. The thermal decomposition of the ternary CR/PA/PVA composite aerogel is relatively delayed compared with the C/PA/PVA aerogel without rectorite (Fig. S8, ESI†). In addition, from the digital photographs of the residues of C/PA/PVA, CR/PA/PVA-RT, and CR/PA/PVA-900 (Fig. S9 and S10, ESI†), CR/PA/PVA-RT has good structural integrity but no flexibility, exhibiting a more rigid, compact, and uniform char than the others. Furthermore, the porous carbon structure is observed from the residue of CR/PA/PVA-RT (Fig. 4(D) and (E)), yet a less pore structure is visible in the burned CR/PA/PVA-900 (Fig. 4(F) and (G)).

The combustion tests combined with TG-DSC measurements and SEM analysis show that the CR/PA/PVA-RT, CR/PA/PVA-300, and CR/PA/PVA-450 composite aerogels demonstrate excellent flame-retardant performances, which can be attributed to the synergistic effects among CR, PA, and PVA in CR/PA/PVA that play a vital role in insulating the CR/PA/PVA aerogel to prevent decomposition. On the one hand, the physicochemical interactions between cellulose nanocrystals and rectorite nanosheets endow the rectorite nanosheets with good dispersion in water and in the PA/PVA matrix and facilitates the formation of uniform coke during the combustion process. On the other hand, the rectorite nanosheets can fill the leakage or defect paths on the ternary network originating from the chemical crosslinking process, thus improving the oxygen barrier performance. In addition, phosphorus (P) in phosphoric acid, added during the synthesis of PA, and a small amount of nitrogen (N) in PA can also contribute to improving the flame-retardant effect of the CR/PA/PVA aerogel (Fig. 3(E)).[34,35] Furthermore, compared with other previously reported mineral-based composite aerogels (mainly montmorillonite) at a heat flux of 50 kW m^{-2}, the CR/PA/PVA-RT composite aerogel in this work has the best flame-retardant properties (Fig. 4(H)).[36–45]

Meanwhile, an alcohol lamp combustion experiment was also performed (Fig. 5, Fig. S10 and Movie S5, ESI†). The C/PA/PVA aerogel (Fig. 5(A)) ignites and begins to melt at the moment when it gets in touch with the flame, the combustion lasted 10 s and appeared an obvious shape change. Besides, the droplet dripping of C/PA/PVA occurred at 21 s. In sharp contrast, CR/PA/PVA-RT (Fig. 5(B)) has a longer burning time and an extraordinary low chance to ignite. Furthermore, it did not get dripping and maintained the original shape after a 90 s-lasting-burning (Movie S5, ESI†). Compared with C/PA/PVA, CR/PA/PVA-900 (Fig. 5(C)) burns more slowly although it also can be ignited. The droplet dripping of CR/PA/PVA-900 occurred at 40 s (Movie S5, ESI†). The above results indicate that the CR/PA/PVA aerogel exhibits much better capability to maintain its structural integrity and shape. Considering the safety of the material, ignition difficulty is of great importance for flame retardation and heat insulation. Moreover, the temperature variation of the aerogel surface which corresponds to the combustion images is recorded using an infrared camera (Fig. 5(D) and Fig. S10, ESI†). It is found that, as the combustion progresses, the surface temperatures of the aerogels gradually increase, the C/PA/PVA aerogel has the highest surface temperature, followed by CR/PA/PVA-900, and CR/PA/PVA-RT is the lowest, indicating that the CR/PA/PVA-RT aerogel possesses not only excellent fire-resistance but also good thermal insulation.

Besides, the thermographic images of the CR/PA/PVA-RT aerogel (ϕ = 1 cm, d = 1.5 cm) placed on a heating plate (150 °C) were recorded. Accordingly, the temperature variation of the aerogel surface at different times was obtained (Fig. 6(A)–(D)). CR/PA/PVA-RT has excellent thermal stability based on above experiments. After being placed on a heating plate for 240 s, the temperature did not change significantly, *i.e.*, from 39.2 °C to 42.7 °C, further demonstrating that CR/PA/PVA-RT has better thermal insulation performance. Thereafter, the thermal conductivity was further measured at 25 °C (Fig. 6(E)), and the CR/PA/PVA-RT aerogel shows a lower thermal conductivity [82.83 mW $(m K)^{-1}$] than that of the C/PA/PVA aerogel [314.8 mW $(m K)^{-1}$]. This difference can be attributed to the architecture of the aerogels, which is described in Fig. 3(H)–(J). Interestingly, the thermal conductivities of the upper and lower layers (denoted as CR/PA/PVA-900-U and CR/PA/PVA-900-L, respectively) of the CR/PA/PVA-900 aerogel are significantly different (Fig. 6(E)). Specifically, the lower and upper layers possess thermal conductivities of 90.1 mW $(m K)^{-1}$ and 322.5 mW $(m K)^{-1}$, which are close to those of CR/PA/PVA-RT and C/PA/PVA, respectively, further confirming the delamination structure of CR/PA/PVA-900. The comparison of our proposed CR/PA/PVA-RT aerogel with several other aerogels reported in the literature has been additionally provided (Fig. 6(F) and Tables S2, S3, ESI†). The simultaneous combination of high elasticity, compressibility, bendability, excellent insulating properties, and superior flame-retardancy has not been observed in traditional aerogels or other porous materials. These advantages, together with the ultralow cost, enable the CR/PA/PVA aerogel to be used as flexible flame-retardant materials in practical applications.
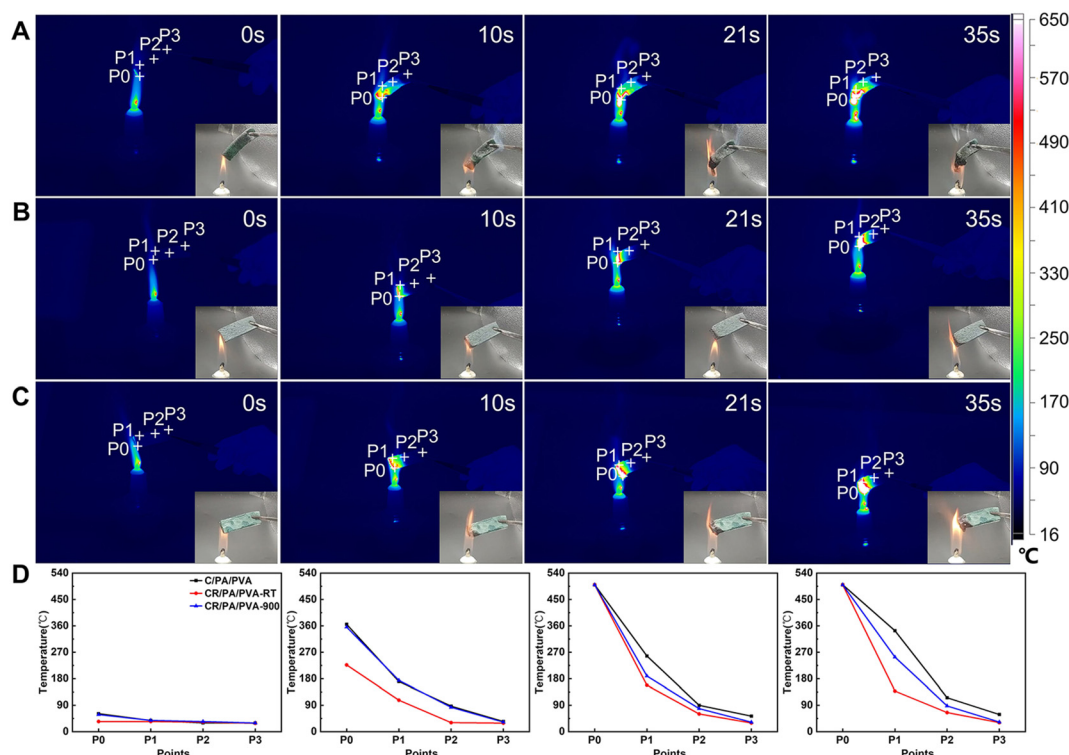
Fig. 5 Infrared image recording temperatures of (A) C/PA/PVA, (B) CR/PA/PVA-RT, and (C) CR/PA/PVA-900 when burned by alcohol (the inset shows the photographs of alcohol lamp combustion experiments of C/PA/PVA, CR/PA/PVA-RT, and CR/PA/PVA-900). (D) Temperature variations at different points in A, B, and C, respectively.

Simulation of interactions among composites

Finally, the interfacial interactions of the CR/PA/PVA aerogel are schematically shown in Fig. 7. With abundant and economical mineral rectorite nanoplatelets as a skeleton, the *in situ* polymerization of the aniline monomer enhances the bonding strength of the interface among rectorite, PA and PVA. The aerogel with an interconnected network could be easily constructed by a freeze-drying technique, which is much simpler, milder and more scalable than most of the previously reported strategies.[47–49] The crosslinking effects of the as-prepared CR/PA/PVA composite aerogel is described as follows:[50–52] the rectorite nanosheets serve as template supports, both PA and PVA can be adsorbed on the surface of rectorite *via* hydrogen bonding, Al–O–C bonding and physical entanglement interactions, so a relatively rigid rectorite skeleton is
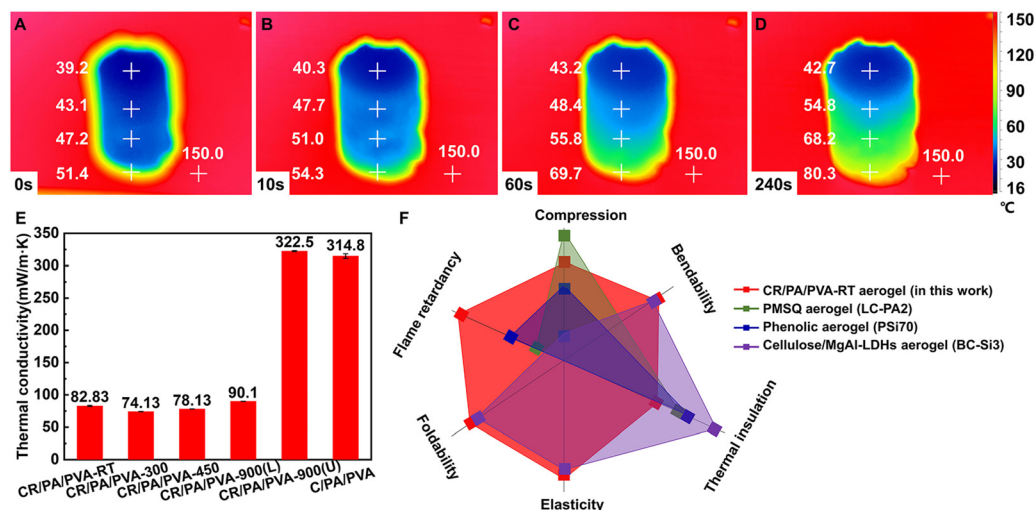

Fig. 6 (A)–(D) Infrared images of the CR/PA/PVA-RT aerogel placed on the heating plate. (E) Thermal conductivities of the as-prepared aerogels. (F) Comparison of the typical properties of CR/PA/PVA-RT with other typical aerogels.[1,13,46]
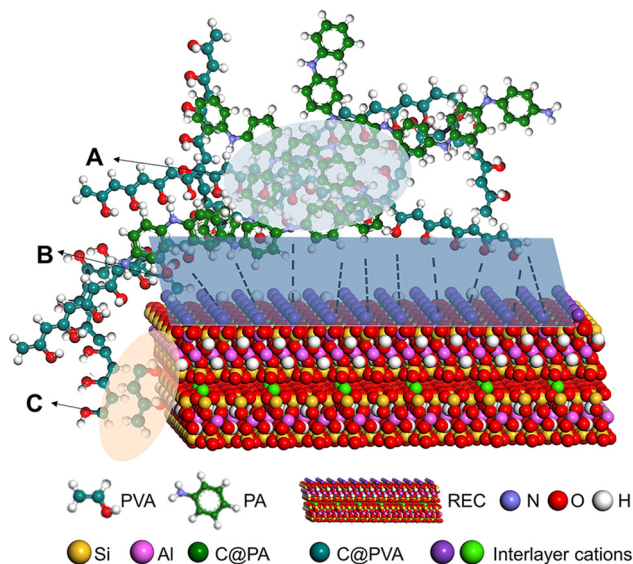
Fig. 7 Schematic diagram of interactions among rectorite nanosheets and polymers (PA and PVA). The representative interaction is shown by the shaded areas of (A)–(C). (A) The physical entanglement interaction between PA and PVA. (B) The hydrogen bond between rectorite and polymers (highlighted by black dots). (C) The Al–OH and Si–OH bonds between rectorite and PVA.

interwoven with two kinds of soft molecular chains, ultimately forming a soft-rigid, crosslinked, ternary framework structure. Overall, such an improvement in the mechanical strength is attributed to the hydroxyl (–OH) and amino (–NH$_2$) groups of the polymers, which can interact strongly with silanols (Si–OH) and aluminols (Al–OH) of rectorite, thus ensuring the strong interfacial interactions between the polymer network and rectorite. These can be confirmed by Fourier transform infrared spectroscopy (FTIR, Fig. S11, ESI†), TGA (Fig. S8, ESI†) and SEM (Fig. 3). For the FTIR spectra of CR/PA/PVA-RT, the intense peaks at 1628 and 1462 cm^{-1} correspond to the quinoid structure and benzenoid rings of PA, respectively. But there is a small shift compared with that of pure PA, demonstrating the strong interaction among the composite aerogel. Moreover, the ternary interpenetrating network structure of the aerogel facilitates the formation of char during the combustion process, thereby forming a dense protective layer to isolate the heat transfer. In brief, in the prepared crosslinked aerogel nanocomposites, one kind of relatively rigid rectorite framework is absorbed with two soft molecular chains, in which both the hydrogen bonding and physical entanglement interactions play crucial roles. It would be promising to regulate and improve the mechanical performance of the resultant aerogel nanocomposites.

Conclusions

In summary, a novel ternary interpenetrating CR/PA/PVA composite aerogel has been designed *via* a direct *in situ* polymerization strategy. A small amount of cellulose nanocrystals was introduced to overcome the severe aggregation of rectorite. The interconnected network structure can be formed among rectorite, PA, and PVA, which plays an indispensable role in improving the flame retardancy and mechanical strength of the obtained aerogels. Consequently, benefitting from the horizontal 3D network structures and radial wave-shape layers, the CR/PA/PVA composite aerogel demonstrates excellent elasticity, foldability, compressibility, and bendability, and high flame retardancy; the peak heat-release rate is as low as 8.3 kW m^{-2}, and the composite aerogel is difficult to ignite. In addition, the resulting composite aerogels exhibit a low thermal conductivity of only 74.13 mW (m K)$^{-1}$, which indicates that the material can provide extended protection against the fire-induced collapse of reinforced concrete structures. The composite aerogels can be integrated with architectural materials and thus have potential in the building, aerospace, and soft decoration applications.

Author contributions

Huaming Yang and Aidong Tang developed the concept for the study and conceived the project. Weimin Xie designed the experiments. Weimin Xie wrote initial drafts of the manuscript. Huaming Yang wrote the final paper. Weimin Xie and Kaixuan Shang performed the preparation and characterization of the samples. Weimin Xie, Jie Wang, Kaixuan Shang, and Hongyun Chen analyzed the corresponding data. Mingjie Wu and Xun Cui offered the help in revising the draft. All the authors discussed the results and commented on the manuscript.

Conflicts of interest

There are no conflicts to declare.

Acknowledgements

Notes and references

1 J. Zhang, Y. Cheng, M. Tebyetekerwa, S. Meng, M. Zhu and Y. Lu, *Adv. Funct. Mater.*, 2019, **29**, 1806407.

2 H. Zhuo, Y. Hu, X. Tong, Z. Chen, L. Zhong, H. Lai, L. Liu, S. Jing, Q. Liu, C. Liu, X. Peng and R. Sun, *Adv. Mater.*, 2018, **30**, 1706705.

3 W. Gan, C. Chen, Z. Wang, J. Song, Y. Kuang, S. He, R. Mi, P. B. Sunderland and L. Hu, *Adv. Funct. Mater.*, 2019, **29**, 1807444.

4 Q. F. Guan, H. B. Yang, Z. M. Han, L. C. Zhou, Y. B. Zhu and C. L. Zhang, *et al.*, *Sci. Adv.*, 2020, **6**, eaaz1114.

5 H. Wang, X. Zhang, N. Wang, Y. Li, X. Feng, Y. Huang, C. Zhao, Z. Liu, M. Fang, G. Ou, H. Gao, X. Li and H. Wu, *Sci. Adv.*, 2017, **3**, e1603170.

6 Y. Si, X. Wang, L. Dou, J. Yu and B. Ding, *Sci. Adv.*, 2018, **4**, eaas8925.

7 J. L. Mohanan, I. U. Arachchige and S. L. Brock, *Science*, 2005, **307**, 397–400.

8 T. Kashiwagi, F. Du, J. F. Douglas, K. I. Winey, R. H. Harris and J. R. Shields, *Nat. Mater.*, 2005, **4**, 928–933.

9 N. Leventis, N. Chandrasekaran, A. G. Sadekar, C. Sotiriou-Leventis and H. Lu, *J. Am. Chem. Soc.*, 2009, **131**, 4576–4577.

10 B. Wicklein, D. Kocjan, F. Carosio, G. Camino and L. Bergström, *Chem. Mater.*, 2016, **28**, 1985–1989.

11 G. Zu, T. Shimizu, K. Kanamori, Y. Zhu, A. Maeno, H. Kaji, J. Shen and K. Nakanishi, *ACS Nano*, 2018, **12**, 521–532.

12 L. Su, H. Wang, M. Niu, X. Fan, M. Ma, Z. Shi and S. W. Guo, *ACS Nano*, 2018, **12**, 3103–3111.

13 Z. L. Yu, N. Yang, V. Apostolopoulou-Kalkavoura, B. Qin, Z. Y. Ma, W. Y. Xing, C. Qiao, L. Bergstrom, M. Antonietti and S. H. Yu, *Angew. Chem., Int. Ed.*, 2018, **57**, 4538–4542.

14 J. Hwang, C. Jo, K. Hur, J. Lim, S. Kim and J. Lee, *J. Am. Chem. Soc.*, 2014, **136**, 16066–16072.

15 Y. Lvov, W. Wang, L. Zhang and R. Fakhrullin, *Adv. Mater.*, 2016, **28**, 1227–1250.

16 J. L. Suter, D. Groen and P. V. Coveney, *Adv. Mater.*, 2015, **27**, 966–984.

17 X. Wang, E. N. Kalali and D. Y. Wang, *Nano. Adv.*, 2016, **1**, 1–16.

18 Z. Hosseinpour Feizi and P. Fatehi, *Cellulose*, 2020, **27**, 3759–3772.

19 K. Peng and H. Yang, *Chem. Commun.*, 2017, **53**, 6085–6088.

20 S. M. Chen, H. L. Gao, X. H. Sun, Z. Y. Ma, T. Ma, J. Xia, Y. B. Zhu, R. Zhao, H. B. Yao, H. A. Wu and S. H. Yu, *Matter*, 2019, **1**, 412–427.

21 S. Jin, Y. Liu, M. Deiseroth, J. Liu, E. H. G. Backus, H. Li, H. Xue, L. Zhao, X. C. Zeng, M. Bonn and J. Wang, *J. Am. Chem. Soc.*, 2020, **142**, 17956–17965.

22 W. Xie, J. Wang, L. Fu, Q. Tan, X. Tan and H. Yang, *Appl. Clay Sci.*, 2020, **185**, 105374.

23 W. Xie, H. Chen, D. He, Y. Zhang, L. Fu, J. Ouyang and H. Yang, *Surf. Coat. Technol.*, 2019, **367**, 118–126.

24 S. T. Bee, A. Hassan, C. T. Ratnam, T. T. Tee, L. T. Sin and D. Hui, *Composites, Part B*, 2014, **61**, 41–48.

25 Z. Zhang, Y. Han, T. Li, T. Wang, X. Gao, Q. Liang and L. Chen, *Synth. Met.*, 2016, **221**, 28–38.

26 F. Hu, J. L. Xu, S. H. Zhang, J. Jiang, B. Yan, Y. C. Gu, M. J. Jiang, S. J. Lin and S. Chen, *J. Mater. Chem. C*, 2018, **6**, 5707–5715.

27 P. M. Naullage and V. Molinero, *J. Am. Chem. Soc.*, 2020, **142**, 4356–4366.

28 W. W. Guo, X. Wang, Y. Pan, W. Cai, W. Y. Xing, L. Song and Y. Hu, *Polym. Adv. Technol.*, 2019, **30**, 1959–1967.

29 Z. N. Hu, S. Q. Yan, X. F. Li, R. C. You, Q. Zhang and D. L. Kaplan, *ACS Nano*, 2021, **15**, 8171–8183.

30 X. Zhang, Q. He, H. Gu, H. A. Colorado, S. Wei and Z. Guo, *ACS Appl. Mater. Interfaces*, 2013, **5**, 898–910.

31 X. N. Wu, X. R. Qian and X. H. An, *Carbohydr. Polym.*, 2013, **92**, 435–440.

32 Z. H. Zhou, Y. B. Yang, Y. Y. Han, Q. Q. Guo, X. X. Zhang and C. H. Lu, *Carbohydr. Polym.*, 2017, **177**, 241–248.

33 H. L. Gao, Y. B. Zhu, L. B. Mao, F. C. Wang, X. S. Luo, Y. Y. Liu, Y. Lu, Z. Pan, J. Ge, W. Shen, Y. R. Zheng, L. Xu, L. J. Wang, W. H. Xu, H. A. Wu and S. H. Yu, *Nat. Commun.*, 2016, **7**, 12920.

34 T. Zhang, H. Yan, M. Peng, L. Wang, H. Ding and Z. Fang, *Nanoscale*, 2013, **5**, 3013–3021.

35 S. Chen, X. Li, Y. Li and J. Sun, *ACS Nano*, 2015, **9**, 4070–4076.

36 H. B. Chen, B. Liu, W. Huang, J. S. Wang, G. Zeng, W. H. Wu and D. A. Schiraldi, *ACS Appl. Mater. Interfaces*, 2014, **6**, 16227–16236.

37 L. Wang, M. Sanchez-Soto and M. L. Maspoch, *Mater. Des.*, 2013, **52**, 609–614.

38 Y. T. Wang, S. F. Liao, K. Shang, M. J. Chen, J. Q. Huang, Y. Z. Wang and D. A. Schiraldi, *ACS Appl. Mater. Interfaces*, 2015, **7**, 1780–1786.

39 Y. T. Wang, H. B. Zhao, K. Degracia, L. X. Han, H. Sun, M. Sun, Y. Z. Wang and D. A. Schiraldi, *ACS Appl. Mater. Interfaces*, 2017, **9**, 42258–42265.

40 N. Wu, F. Niu, W. Lang and M. Xia, *Carbohydr. Polym.*, 2019, **221**, 221–230.

41 X. L. Li, M. J. Chen and H. B. Chen, *Composites, Part B*, 2019, **164**, 18–25.

42 H. B. Chen, Y. Y. Ao, D. Liu, H. T. Song and P. Shen, *Ind. Eng. Chem. Res.*, 2017, **56**, 8563–8567.

43 X. Y. Zhou, H. R. Jin, T. T. Xu, J. B. Wang, Y. Zhu, S. J. Ding, T. Hu, S. Yun and J. Chen, *Appl. Clay Sci.*, 2020, **184**, 105402.

44 L. Wang, D. A. Schiraldi and M. Sánchez-Soto, *Ind. Eng. Chem. Res.*, 2014, **53**, 7680–7687.

45 H. B. Chen, P. Shen, M. J. Chen, H. B. Zhao and D. A. Schiraldi, *ACS Appl. Mater. Interfaces*, 2016, **8**, 32557–32564.

46 X. Luo, J. Shen, Y. Ma, L. Liu, R. Meng and J. Yao, *Carbohydr. Polym.*, 2020, **230**, 115623.

47 S. Deville, E. Saiz, R. K. Nalla and A. P. Tomsia, *Science*, 2006, **311**, 515–518.

48 E. Munch, M. E. Launey, D. H. Alsem, E. Saiz, A. P. Tomsia and R. O. Ritchie, *Science*, 2008, **322**, 1516–1520.

49 H. Le Ferrand, F. Bouville, T. P. Niebel and A. R. Studart, *Nat. Mater.*, 2015, **14**, 1172–1179.

50 Z. H. Zhang, Z. Y. Chen, Y. H. Tang, Y. T. Li, D. Q. Ma, G. D. Zhang, R. Boukherroub, C. F. Cao, L. X. Gong, P. G. Song, K. Cao and L. C. Tang, *J. Mater. Sci. Technol.*, 2022, **114**, 131–142.

51 K. Y. Guo, Q. Wu, M. Mao, H. Chen, G. D. Zhang, L. Zhao, J. F. Gao, P. G. Song and L. C. Tang, *Composites, Part B*, 2020, **193**, 108017.

52 Z. R. Yu, M. Mao, S. N. Li, Q. Q. Xia, C. F. Cao, L. Zhao, G. D. Zhang, Z. J. Zheng, J. F. Gao and L. C. Tang, *Chem. Eng. J.*, 2021, **405**, 126620.